Crack-reduced alumina/aluminum titanate composites additive manufactured by laser powder bed fusion of black TiO_{2-x} doped alumina granules

Stefan Pfeiffer [a,b,*], Kevin Florio [c], Malgorzata Makowska [d], Federica Marone [d], Sena Yüzbasi [a], Christos G. Aneziris [b], Helena Van Swygenhoven [d], Konrad Wegener [c], Thomas Graule [a,b]

[a] *Laboratory for High Performance Ceramics, Empa – Swiss Federal Laboratories for Materials Science and Technology, Überlandstrasse 129, 8600 Dübendorf, Switzerland*
[b] *Institute of Ceramic, Glass and Construction Materials, TU Bergakademie Freiberg, Agricolastraße 17, 09599 Freiberg, Germany*
[c] *Institute of Machine Tools and Manufacturing, ETH Zürich, Leonhardstrasse 21, 8092 Zurich, Switzerland*
[d] *Photon Science Division, Paul Scherrer Institut, 5232 Villigen PSI, Switzerland*

ARTICLE INFO

ABSTRACT

Laser powder bed fusion is an emerging industrial technology, especially for metal and polymer applications. However, its implementation for oxide ceramics remains challenging due to low thermal shock resistance, weak densification and low light absorptance in the visible or near-infrared range. In this work, a solution to increase the powder absorptance and to reduce cracking during laser processing of alumina parts is given. This is achieved by the use of a homogeneously dispersed and reduced titanium oxide additive (TiO_{2-x}) within spray-dried alumina granules leading to formation of aluminum titanate with improved thermal shock behavior during powder bed fusion. The impact of different reduction temperatures on powder bed density, flowability, light absorption and grain growth of these granules is evaluated. Crack-reduced parts with a density of 96.5%, a compressive strength of 346.6 MPa and a Young's modulus of 90.2 GPa could be manufactured using powders containing 50 mol% (43.4 vol%) TiO_{2-x}.

1. Introduction

The industrial usage of laser powder bed fusion (also known as selective laser melting) to produce ceramic parts is restricted due to the brittle nature of this material group. However, it offers a great potential to produce highly complex prototypes and small series by expanded boundaries for design engineers. Parts could be manufactured with high accuracy and short lead times, potentially avoiding costly hard-machining and thermal post processing which is both energy and time consuming.

Several approaches to overcome the problems of low thermal shock resistance and weak densification of oxide ceramics were already tested, however, they were only partly successful in combining a high accuracy, suitable mechanical properties and a total freedom of design [1]. The main-focus of most of these approaches was hereby on optimization of the laser processing. Process conditions were adjusted by the use of

different lasers [2–7]), various laser scanning strategies [8] and pre-heating strategies [3,9–11]. However, the change of the material composition should be also considered as a suitable approach to establish powder bed fusion – laser beam (PBF-LB) by improving the properties of the ceramic parts [2,5,12]. Furthermore, the combination of different materials offers the chance to control the powder absorptance [4]. Aluminum oxide shows low absorption in the visible or near infrared range (3% absorption at 1064 nm [13]). To increase the powder absorptance of the laser light in this wavelength range, carbon [14], [15–18], SiC [17], Fe_2O_3 [4,19,20] and MnO_2/Mn_2O_3 [21–23] were formerly added to oxide particles and proved to be suitable absorbers. The mixing of different powders can be done for example by using spray granulation, which will be beneficial to achieve a suitable flowability and powder bed density even by using nano- or submicron powders [19]. It was reported that only a sufficiently high powder bed density leads to a high density of the final laser processed parts [24,25]. Spray

---

granulation also provides the possibility of a homogeneous particle distribution and an optimized layer thickness of the powder bed. This method was previously applied by Juste et al. [14], Mapar et al. [26,27], Verga et al. [18], Liu et al. [28], Pfeiffer et al. [19,23] and Florio et al. [4, 22] in terms of powder bed preparation.

Crack formation is a main issue in PBF-LB of aluminum oxide due to low thermal shock resistance of the material and the high thermal stresses generated during melting and re-solidification processes. The in-situ formation of aluminum titanate from aluminum oxide and titanium oxide during laser processing has a great potential to reduce the number of cracks formed by thermal stresses in the melt-grown ceramics [29–31]. Aluminum titanate has a low thermal expansion coefficient and therefore, an optimized thermal shock behavior [32]. Furthermore, it offers a low Young's modulus beneficial for the thermal shock resistance [33] and improves the poor fracture toughness of Al_2O_3 through crack deflection and residual compressive stress regions [34,35]. The local residual stresses and microcracks are usually generated by the difference in thermal expansion coefficients between Al_2O_3 and Al_2TiO_5 [34].

Crack-free parts containing alumina and aluminum titanate could be already manufactured by Directed Energy Deposition (DED) [29]. The in-situ formed phase was mainly found as a matrix at α-alumina grain boundaries consisting of Al_2TiO_5 and $Al_6Ti_2O_{13}$ [31]. Cracks could be suppressed proportionally to the amount of additives used up to 50 wt% [29]. However, the best flexural strength was achieved for amounts of additive below 10 wt% due to the low mechanical strength of aluminum titanate [30]. Higher amounts led to a strong decrease in flexural strength, hardness and fracture toughness accompanied by an increase of the porosity up to 5% [30]. An addition of 5 wt% TiO_2 gave the highest fracture toughness according to Wu and Huang et al. [30,31]. In studies on laser cladding of Al_2O_3-TiO_2, crack-free layers with low porosity and an excellent bonding behavior with the metallic substrate were produced [36–38]. The powder with an addition amount of 13 wt% TiO_2 to Al_2O_3 was fed to the melt pool in the form of spray dried granules [36] or prior to laser processing by pressing on the substrate [38].

The bandgap of titanium oxide is too large (3.4 eV for anatase [39]) to improve the absorptance of aluminum oxide powder in the visible or near-infrared laser light. However, reduction of TiO_2 to black titanium oxide offers a solution for this problem by significantly changing its optical properties. Reduced TiO_{2-x} is normally used due to an enhanced photocatalytic effect [40,41] and offers not only a smaller bandgap (depending on the reduction grade), but also shows improved electrical conductivity [42]. This enables the use of only titanium oxide as an effective dopant for PBF-LB with visible or near-infrared laser light. Some of the techniques suitable to produce TiO_{2-x} (Magnéli phases) are pulsed UV laser irradiation in acetonitrile [43], the use of a zirconium getter [42], a treatment within pure hydrogen [44] or a N_2/H_2 mixture [45], a treatment with the aid of molten reduced aluminum [46], the use of a carbothermal reduction under constant argon flow [47] or even a high-pressure treatment in hydrogen [40]. However, treatment temperatures have to be carefully evaluated, since untreated titania particles are only available as nano- or submicron particles and therefore, they show sintering and rapid grain coarsening already at low temperatures [48,49].

In the present work, customizing of material composition by addition of reduced black titanium oxide to spray-dried alumina granules is shown to solve both problems of low powder absorptance and severe crack formation during laser processing of aluminum oxide. Nano titanium oxide is homogeneously dispersed within the granules and reduced under argon/hydrogen atmosphere at high temperatures prior to PBF-LB. The formation of the secondary phase aluminum titanate during laser processing led to crack-reduced laser manufactured parts.

2. Experimental

2.1. Starting materials

Submicron α-alumina Taimicron TM-DAR (Taimei Chemicals Co. LTD, Japan) and micron-sized α-alumina AA3 (Sumitomo, Chemical Co. LTD, Japan) were used to achieve multimodal distributions of alumina within the granules and therefore, to increase the powder bed density according to McGeary [50] and Pfeiffer et al. [19,23]. Furthermore, Aeroxide TiO_2 P25 nanoparticles (Evonik Industries AG, Germany) were incorporated within the granules during spray drying. The absolute densities, specific surface area and BET average particle size of the used powders can be found in Table 2. Ammonium citrate dibasic p.a. 98% (Sigma Aldrich Corp., USA) was utilized as a surfactant, since it guarantees a homogeneous dispersion of all particles by creating a negatively charged surface [19,51].

The absolute density of the TiO_2 powder was evaluated by helium pycnometry (AccuPyc II 1340, Micromeritics, USA). BET (Brunauer–Emmett–Teller) measurements (SA 3100, Beckman Coulter, Germany) gave the specific surface area (SSA). The powder was degassed with synthetic air for two hours at 180 °C (SA-PREP Surface Area Outgasser, Beckman Coulter, Germany) before performing the SSA measurement. The corresponding BET average particle size was calculated from the measured absolute density and SSA according to the Sauter mean diameter [52]. The surface potential of the particles was determined by electroacoustic zeta potential measurements with a ZetaProbe Analyzer (Colloidal Dynamics, USA). The measurements were performed at different pH-values with an equilibration delay of 30 s. A 0.1 molar solution of HCl (Carl Roth GmbH + Co. KG, Germany) and a 0.1 molar NaOH (Sigma Aldrich Corp., USA) were titrated to adjust the pH of the utilized aqueous 5 wt% suspensions. Dielectric constants were taken from literature [53]. A saturation amount of surfactant on the particle surfaces was evaluated by these measurements. This amount of dispersant (2.6 wt%) was mixed with the powder to conduct a proper dispersion in Nanopure water. The dispersion was made by a combination of roll milling for 24 h and vibration milling for 20 min with a vibrational frequency of 30 Hz (Retsch MM301, Retsch GmbH, Germany) using 0.4 mm ZrO_2 milling balls (Tosoh Corporation, Japan). Volume based particle size distributions of the dispersed starting material was measured in water by laser diffraction (LS 13320, Beckman Coulter GmbH, Germany) and dynamic light scattering (ZetaSizer Nano ZS, Malvern Panalytical LtD, United Kingdom). The required refractive indices and extinction coefficients for the size measurements were taken from DeVore [54] for TiO_2.

2.2. Spray granulation, thermal treatment and mixing with coarse alumina

Spray granulation was performed in the Mini spray dryer B-290 (Büchi Labortechnik AG, Switzerland) with an ultrasonic atomizer in co-current mode. The slurry was delivered to the nozzle by a peristaltic pump and left stirring to prevent demixing. The following process parameters were used: an inlet temperature of 140 °C, an outlet temperature of ca. 100 °C, an air flow rate within the spraying apparatus of 25 m^3/h, a nozzle frequency of 60 kHz and a slurry feed rate of ca. 1.1 ml/min. The slurry used for spray drying of the different granules consisted of six components: (1) aluminum oxide, (2) titanium oxide, (3) ammonium citrate dibasic (dispersant), (4) PEG 35000 (binder), (5) Nanopure water (solvent) and (6) ZrO_2 milling balls. Table 1a summarizes the combinations of the different aluminum oxide and titanium oxide starting powders in the slurry.

The aluminum oxide powders (1) were dispersed in water (5) on a roller bench for 24 h by the use of ammonium citrate dibasic (3) and milling balls (6) as described into more details in [19,23]. The titanium oxide powders were dispersed as explained in chapter 2.1. The binder PEG 35000 (Sigma Aldrich Corp., USA) (2 wt% (6.2 vol%)) was added to

Table 1

Combinations of aluminum oxide and titanium oxide starting powders in the slurry used for spray drying.

Final amount of TiO₂ within spray-dried granules	Ratio of starting powders					
	Al₂O₃ AA3		Al₂O₃ Taimicron TM-DAR		Aeroxide TiO₂ P25	
	vol%	wt%	vol%	wt%	vol%	wt%
1 vol%	71.9	72.1	27.1	26.8	1.0	1.0
14.3 vol%	72.6	72.5	13.1	12.9	14.3	14.6
68 mol% (61.9 vol%)	38.1	37.5	–	–	61.9	62.5

the micron-sized alumina AA3 after rotating for 1 h and kept rolling for 23 h. After dispersing, the individual slurry components were mixed and additionally homogenized for 4 h on a roller bench. The milling balls were removed before spray drying. Granules with 1 vol%, 14.3 vol% and 68 mol% (61.9 vol%) TiO₂ were sprayed with an ultrasonic power of 11, 7 and 8 W. respectively. Overheating of the ultrasonic nozzle was prevented by a stream of compressed air. The process parameters were kept constant during spray drying. The final granule separation was carried out in a cyclonic collector and an additional screening step with a 230 mesh (63 μm) sieve (Retsch GmbH, Germany). The yield of the spray drying process was calculated by the fraction of the weight of received granules to the weight of all solid contents in the dispersion.

Granules were thermally treated in the tube furnaces Carbolite STF 16/610 and Carbolite CTF 17/300 (Carbolite Gero GmbH & Co. KG, Germany) in Ar/H₂ (98/2%) atmosphere. The applied maximum temperature varied from 1000 up to 1600 °C. Dwell times of 2 h were used with a heating rate of 2 K/min. After thermal treatment, the granules were screened with a 120 mesh (125 μm) sieve. To reach a final TiO₂₋ₓ content of 0.7 vol%, 10 vol% and 50 mol% (43.4 vol%), 30 vol% coarse alumina AA18 was mixed with the granules on a roller bench during 1 h. This procedure breaks the sintering necks in between sintered granules, making an easy flowable medium and increasing the powder bed density [23]. The amount of 50 mol% (43.4 vol%) of aluminum oxide and titanium oxide was proposed to achieve pure aluminum titanate in the case of a fully completed reaction during laser processing. Prior to the thermal treatment in the tube furnaces, a thermal gravimetric analysis (Netzsch STA 449F3 Jupiter, Netzsch Gerätebau GmbH, Germany) in argon/hydrogen atmosphere was performed to evaluate the minimum temperature necessary to reduce the TiO₂ particles. The measurement was conducted with a heating rate of 2 K/min up to a temperature of 1470 °C. Furthermore, the derivation of the mass loss using average values of 50 measurement points was calculated to facilitate the evaluation of this critical reduction temperature.

2.3. Granule characterization

2.3.1. Apparent and tapped density, flowability and particle size distribution

The quality of the powders was evaluated by apparent density measurements (PTL Dr. Grabehorst GmbH, Germany) according to the standard DIN EN ISO 23145–2 and tapped density measurements by applying a jolting volumeter (JEL STAVII, J. Engelsmann AG, Germany). The sample was tapped 1000 times with a displacement of 3 mm in compliance to EN ISO 787–11. Relative densities were calculated as fractions of the apparent and tapped density over the absolute powder density. The ratio of tapped density divided by apparent density (Hausner ratio) enabled a flowability grading of the powders. The Hausner ratio relates to frictional conditions in a moving powder [55, 56] and is a static measurement by use of powder gravity [57]. Values below 1.25 should guarantee a fair flowability for the PBF-LB process [15,17,56,58]. The dynamic flow behavior of different granules during agitation was evaluated using a Revolution Powder Analyzer (PS Prozesstechnik GmbH, Switzerland). It is an appropriate way to simulate stress and flow conditions during recoating for PBF-LB. 10 ml of powder was filled into a 25 ml drum equipped with two glass windows to guarantee a direct capture of the flow behavior by a CCD camera (15

images/s). The drum was brought into rotation (0.6 rounds/min) and the characteristic values of the avalanche angle (angle of powder when the avalanche occurs) were automatically calculated by the integrated software after a preparation time of 30 s. A low angle implements a good powder flowability and an angle bigger than 60° is critical to achieve a suitable flowability for powder recoating [59]. Three measurements were performed for each powder evaluating at least 127 avalanches within each run to ensure a repeatability of the results. The average standard deviations for apparent density, tapped density, Hausner ratio and avalanche angle were 1.3%, 0.5%, 1.4% and 11.4%, respectively. Particles size distributions of the powders were monitored by laser diffraction with the LS 13320 in isopropanol including the characteristic values for d_{10}, d_{50} and d_{90}.

2.3.2. Electron microscopy and absorptance measurement

The shape of the granules and the impact of thermal treatment in Ar/H₂ on the morphology were visualized by the Scanning Electron Microscopy (VEGA3 Tescan, Tescan instruments, Czech Republic). Prior to this analysis, the powder was distributed with compressed air on an adhesive carbon tab and then sputtered with Au-Pd. Qualitative light absorption measurements in a wavelength range of 300–1500 nm (in 2 nm steps) employing the Kubelka-Munk method [60,61] were performed with the Shimadzu 3600 UV–VIS–NIR spectrophotometer (Shimadzu Corporation, Japan). More details to the Kubelka Munk method including the calculation of the ratio of the arbitrary constants of absorption (absorption coefficient K) and scattering (scattering coefficient S) by measuring the reflectance of the sample can be found in [23].

2.4. Laser processing

Laser powder bed fusion of the customized powders was done in an experimental, in-house built PBF-LB machine under air flow [4]. Two types of lasers were used.

Based on the results for doping amounts below 1 vol% Fe₂O₃ [4,19, 20] and MnO₂/Mn₂O₃ [23] doped aluminum oxide, a green (532 nm) pulsed (1.5 ns) laser with a nominal average output power of 5 W and a pulse repetition rate of 300 kHz (GLPM-5, IPG Photonics, USA) was used for the laser processing of the lowest doping amount of 0.7 vol% TiO₂₋ₓ. A continuous wave IR fiber laser (redPOWER R4 200 W, SPI lasers, UK) was also tested with this powder, but a successful consolidation of the part could not be achieved due to low absorptance. This enables the comparison of parts produced from powders doped with reduced titanium oxide with parts from powders doped with the other two dopants. The laser parameters used during processing were a spot diameter of 130 μm, a hatch space of 135 μm, a layer thickness of 40 μm and a laser power of 5.75 W (measured by a power meter). The substrate for laser processing was an alumina foam with 70–77% porosity.

For the processing of the powders containing higher additive amounts the continuous wave IR fiber laser could be used due to a higher powder absorptance. This higher absorptance at a wavelength of 1070 nm compared to 532 nm was confirmed by the Kubelka Munk method as shown in the results and discussion section. The fiber laser is used by most commercial PBF machines due to reliability. The spot size can be smaller in comparison to a CO₂ laser, since it depends on the used wavelength. Furthermore, melt pool cavities (key holes) induced by material evaporation due to high peak intensities of pulsed lasers should

be avoided. The laser features following characteristics: a wavelength of 1070 nm and a maximum nominal output power of 200 W. A spot size of 90 μm, a hatch distance of 175 μm and a layer thickness of 40 μm were used for laser processing. The substrate for laser processing was a Sn60Pb40-coated steel following the same preparation procedure shown in Verga et al. [18].

2.5. Characterization of PBF-LB manufactured parts

The shape of the PBF-LB printed ceramic parts was imaged by optical microscopy (SteREO Discovery.V20, Carl Zeiss Microscopy, Germany). The internal structure of the parts was illustrated by the optical microscope Keyence VHX 5000 (Keyence Corporation, Japan) and the SEM VEGA3 Tescan. Before the microstructure imaging, the samples were cold embedded in a resin (CaldoFix-2, Struers GmbH, Switzerland) and the cross-sections were ground and polished (down to a minimum diamond suspension of 1 μm).

The density according to the Archimedes principle was determined using water as liquid medium. The relative density of the parts was calculated based on the absolute densities of crushed PBF-LB printed parts. The compressive strength was measured using cylinders with a diameter of ca. 5 mm and a length of ca. 8 mm. The samples were polished up to a 5 μm finish prior to the compression tests. The compression tests were performed using the Instron 8801 servohydraulic testing systems (Illinois Tool Works Inc., USA). The uniaxial compressive strength σ was calculated using the applied force F and the cross-sectional area A of the cylinders as follows:

$$\sigma = \frac{F}{A} = \frac{F}{\frac{1}{4}d^2\pi} \tag{1}$$

The Young's modulus of the laser processed samples was measured using the ultrasonic method. Each sample was ground plane-parallel prior to the measurement to enable a good coupling. Honey was used as a couple medium between sensors and sample. The sound velocity of longitudinal (c_L) and transverse (c_T) waves were created by the ultrasonic measuring device Panametrics 5900 PR (Olympus K.K., Japan) by the use of 4 and 0,5 MHz, respectively, and calculated from material thickness measurements and time of flight measurements evaluated by the equipped software Ultrasound Imaging System Version 2.2.c. The Young's modulus E can be determined evaluating the material density ρ as follows:

$$E = 4\rho c_T^2 \frac{\frac{3}{4} - \left(\frac{c_T}{c_L}\right)^2}{1 - \left(\frac{c_T}{c_L}\right)^2} \tag{2}$$

X-ray tomographic microscopy was performed at the TOMCAT beamline of the Swiss Light Source. Tomography scans were performed using a standard setup for full field tomography composed of a 100 μm-thick LuAG:Ce scintillator, an optical microscope with 4x magnification and a sCMOS camera, which provides a field of view of 4.2 mm × 3.5 mm with 1.625 μm pixel size. The energy of the X-ray beam was 25 keV. 1501 projections were acquired over 180° with 280 ms exposure time per projection. 3D imaging of $2\times2x2$ mm^3 sized cubes allowed to visualize the microstructure with a spatial resolution of about 3 μm. Part density and crack density values were evaluated for the laser processed parts from the tomography visualizations. The relative error estimated for the density measurements was ca. 0.1%.

The reduced granules were characterized using the PANalytical X′Pert PROh–2 h (PANalytical, Netherlands) scan system equipped with a Johansson monochromator (Cu Kα1 radiation, 1.5406 Å) and a X′Celerator linear detector. The scans were collected in the 2θ range of 5 − 80° with a step size of 0.016° and a scanning speed of 0.021° s − 1. X-ray powder diffraction measurements on ground PBF-LB printed parts were performed in Bragg–Brentano geometry using a Bruker AXS D8 ADVANCE diffractometer (Bruker Corporation, USA) equipped with Cu-Kα X-ray source. The data was acquired in 2θ range of 5–120° with a step

of 0.02° and a 1 s exposure time per step. The TOPAS Bruker AXS software was used for identification of crystallographic phases.

3. Results and discussion

3.1. Dispersion of starting powders in water

The used aluminum oxide powders AA18, AA3 and Taimicron TM-DAR were already analyzed in terms of absolute densities, the specific surface area (SSA) and the resulting BET average particle size [19,23]. For the Aeroxide TiO$_2$ P25 nanoparticles, a specific surface area of 50.0 m^2/g was measured. A value of 4.1 g/cm^3 was taken as the absolute density of these particles. Therefore, a BET average particle size of 29.3 nm could be calculated. The absolute densities, the SSA and the BET average particle size of the used raw powders are summarized in Table 2.

Ammonium citrate dibasic was previously already shown to be a suitable dispersant for the micron-sized AA3 and submicron-sized Taimicron TM-DAR. More details on the zeta potential measurements and the consecutive dispersing step can be found in [19,23]. Fig. 1a shows the zeta potential of the Aeroxide TiO$_2$ P25 nanoparticles in water as a function of pH value and various citrate concentrations. A shift of the isoelectric point from 6.7 to 2.7 occurs by the addition of ammonium citrate dibasic (Fig. 1b), since citrate causes an exchange of hydroxyl groups with carboxylate ions by adsorption on the TiO$_2$ particle surfaces and therefore, causes an increase of the zeta potential [51]. The evaluated saturation amount (monolayer of citrate anions fully covers the surface of the particles) of ammonium citrate dibasic was 2.6 wt% (6.4 vol%). By addition of this saturation amount, the zeta potential was below − 50 mV for pH values bigger than 5. For higher pH values a successful electrostatic stabilization of the particles by a strongly negative charged surface should be given, which makes the particles suitable for multimodal dispersions containing aluminum oxide.

Fig. 1c, d illustrate volume based particle size distributions of TiO$_2$ nanoparticles in water using the saturation amount of ammonium citrate dibasic. Attractive van der Waals forces have high impact on the TiO$_2$ nanoparticles due to decreasing gravitation forces [62]. Therefore, only vibration milling led to agglomerations of up to ca. 850 nm measured by laser diffraction. The higher energy input by an additional roll milling step for 24 h diminished the amount of bigger agglomerates. Dispersing experiments with a solid loading of 5 vol% TiO$_2$ nanoparticles in water and 0.4 mm milling balls gave the best results (Fig. 1c, d), since a higher solid loading of 10 vol% led to an extremely raised viscosity of the slurry. The d$_{50}$ of 56 nm measured by dynamic light scattering was close to the BET average particle size of 29.3 nm. Laser diffraction shows in general slightly bigger values due to the given diffraction limit.

The volume based particle size distributions (DLS and LD) of the used alumina powders dispersed in water were already presented [19,23]. For the powders AA3 and AA18, the particle size distributions were only evaluated by laser diffraction, since the particle size was at the upper measurement limit of the dynamic light scattering device. The micron-sized AA3 and the submicron-sized Taimicron TM-DAR could be well dispersed by ammonium citrate dibasic with no agglomerates and a

Table 2
Absolute densities, specific surface area and BET average particle size of raw powders.

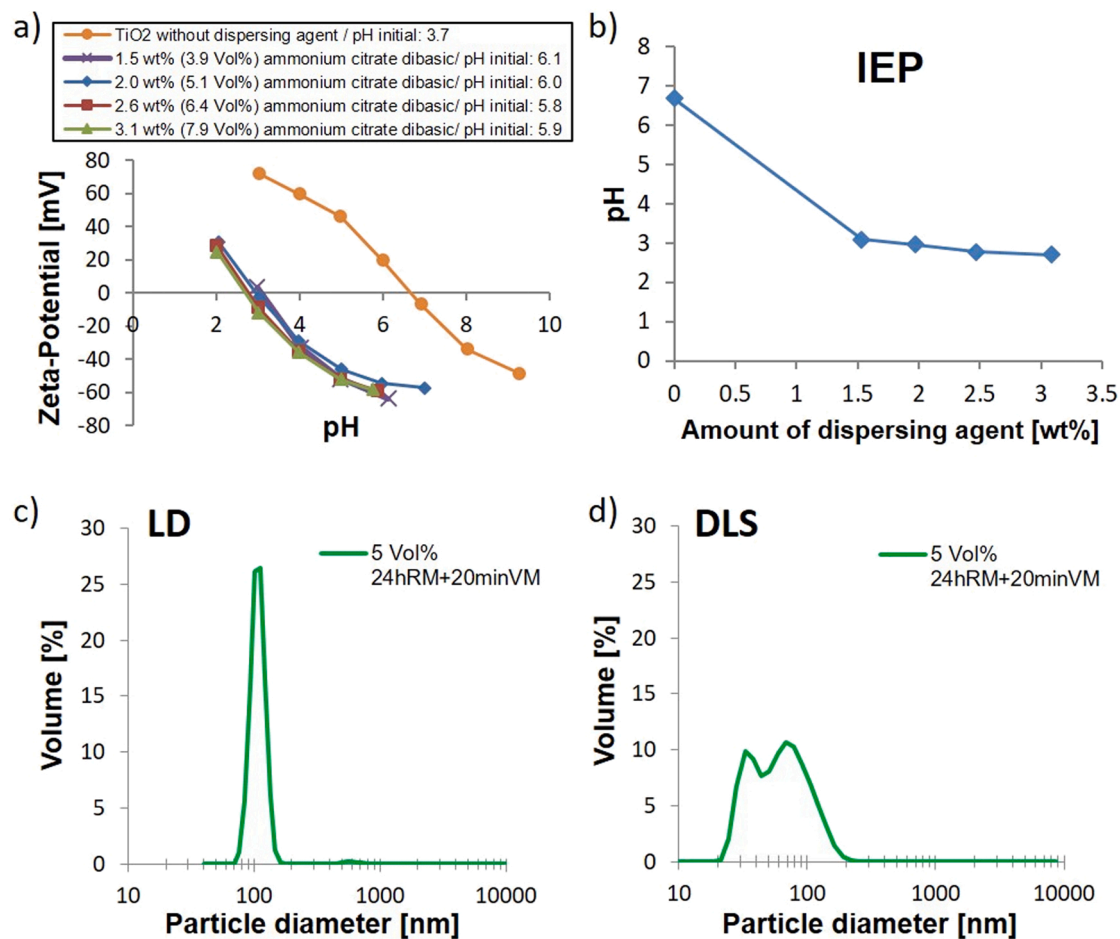| Raw material	Al$_2$O$_3$ AA18	Al$_2$O$_3$ AA3	Al$_2$O$_3$ Taimicron TM-DAR	Aeroxide TiO$_2$ P25
Absolute density [g/cm^3]	3.99	4.01	3.95	4.1
Specific surface area [m^2/g]	< 0.1	0.4	11.8	50.0
BET average particle size [nm]		3700	128.8	29.3

Fig. 1. a) Zeta potential of TiO_2 particles as a function of pH value and various citrate concentrations. b) pH_{IEP} of TiO_2 suspensions as function of ammonium citrate dibasic addition. Volume based particle size distributions of TiO_2 nanoparticles in water determined by c) laser diffraction (LD) and d) dynamic light scattering (DLS).

Table 3
d_{10}, d_{50} and d_{90} of volume based particle size distributions of dispersed powders in water determined by dynamic light scattering (DLS) and Laser diffraction (LD).

Powder	Al_2O_3 AA18	Al_2O_3 AA3	Al_2O_3 Taimicron TM-DAR		Aeroxide TiO_2 P25	
Measurement method	LD	LD	LD	DLS	LD	DLS
d_{10}	10.9 μm	2.23 ± 0.01 μm	109.1 ± 2.0 nm	132.6 ± 2.7 nm	86.0 ± 0.1 nm	28.7 ± 9.2 nm
d_{50}	18.6 μm	3.01 ± 0.05 μm	148.2 ± 1.0 nm	201.2 ± 3.6 nm	102.1 ± 0.1 nm	56.0 ± 13.2 nm
d_{90}	26.1 μm	4.38 ± 0.27 μm	212.2 ± 1.4 nm	294.5 ± 12.2 nm	121.3 ± 0.4 nm	106.4 ± 4.7 nm

uniform distribution [19].

The results for the characteristic values of d_{10}, d_{50} and d_{90} of the dispersed powders are summarized in Table 3.

3.2. Thermal treatment of Al_2O_3/TiO_2 granules under argon/hydrogen atmosphere

Fig. 2a, b depicts a thermal gravimetric analysis to evaluate the minimum temperature necessary to reduce the TiO_2 nanoparticles in argon/hydrogen atmosphere. There was a significant mass loss as a result of TiO_2 to TiO_{2-x} reduction after 980 °C. The measured mass loss between 200 and 980 °C was only 0.67 wt%, whereas the total mass loss up to the maximum temperature of 1470 °C was 4.79 wt%. Furthermore, a color change occurs in the powder from white to black above 980 °C as a result of the reduction. The same phenomenon was also observed in the spray dried granules containing 1 vol% of TiO_{2-x} (Fig. 2c). The powder changes the color from pure white to dark-grey upon thermal treatment in Ar/H_2. This enables the use of reduced

titanium oxide as an effective dopant for laser processing in the visible or near-infrared range of the light.

The microstructure of the granules containing 1 vol% of TiO_{2-x} changes upon thermal treatment with the maximum temperatures of 1400 °C and 1600 °C (dwell times: 2 h) (Fig. 3). The spray-dried granules without thermal treatment have a mostly spherical appearance. Using 1400 °C, the sintering of the grains within the predominately alumina granules was at an early stage. A final complete sintering of the granules was reached at 1600 °C (dense microstructure with no visible porosity). The presence of the TiO_2 dopant triggered a uniform grain growth within the alumina granules. However, the higher treatment temperature of 1600 °C led to more sintering necks between the granules (satellite formation). A similar impact on the sintering behavior on TiO_2-doped alumina in air atmosphere was previously reported by Sathiyakumar and Gnanam [63]. They found that TiO_2 is effective for grain growth promotion in Al_2O_3 up to a doping amount of 0.2 wt% and achieved high densities already at maximum sintering temperatures of 1400 °C. With higher additive amounts (contents of up to 4.0 wt%), the
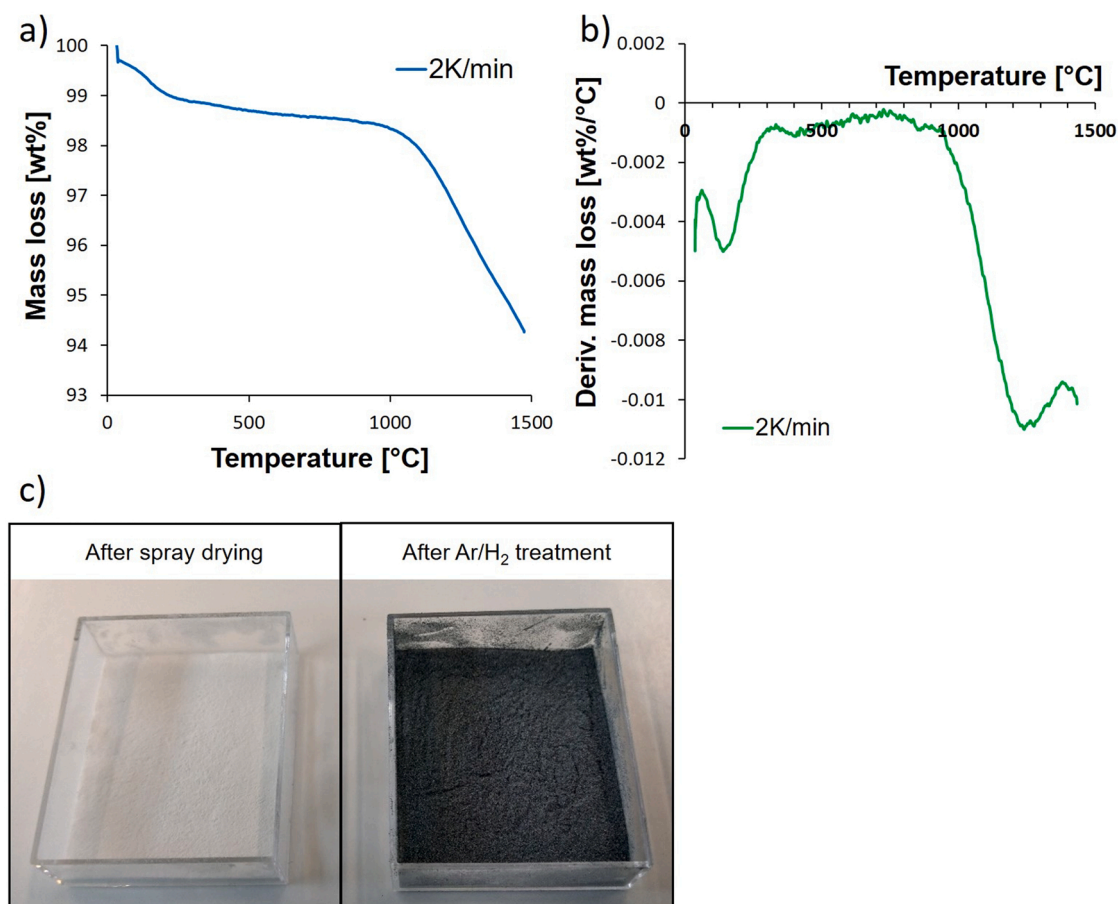
Fig. 2. Thermal gravimetric analysis to evaluate the minimum temperature necessary to reduce the TiO_2 nanoparticles to TiO_{2-x} in argon/hydrogen atmosphere by a) mass loss and b) derivation of the mass loss. c) Optical appearance of spray dried granules containing 1 vol% of TiO_{2-x} before and after thermal treatment in Ar/H_2.

sintering rate and the grain sizes decreased.

The spray dried granules containing 14.3 vol% of TiO_{2-x} are less spherical than the granules sprayed with a lower doping amount of 1 vol %. Sintering of the particles was not visible after a thermal treatment in Ar/H_2 with a maximum temperature of 1000 °C. The treatment at 1200 °C led to an early stage sintering, which was enhanced at 1300 °C and 1400 °C. The depletion of oxygen by reduction of TiO_2 to TiO_{2-x} was visible by micron-size porosity appearing on the surface of the granules at the higher treatment temperatures.

The granules containing 68 mol% (61.9 vol%) of TiO_{2-x} showed an even lower sphericity than the other granules after spray drying. This detrimental effect on the particle shape is due to the enhanced movement of the nano-sized TiO_2 particles in multimodal particle combinations [64]. The high amount of the fully dispersed nanoparticles is very versatile without intergranular interactions within the droplets and packs densely at the shell [65]. Furthermore, the sintering temperature of these granules was reduced. A thermal treatment in Ar/H_2 at 1000 °C showed already an early stage sintering and micron-size porosity due to the reduction of oxygen was visible in the SEM images. Rapid grain growth occurred at the higher temperatures of 1300 °C and 1400 °C. In comparison, pure TiO_2 systems showed sintering and rapid grain growth already at lower temperatures. Dittmann et al. [48] measured that shrinkage of pure nano-sized titania was initiated at 500 °C in air atmosphere. At 780 °C, the whole sample was transformed from anatase to pure rutile and starting from 800 °C, rapid grain growth appeared. At 900 °C, the whole sample was already completely sintered. Mazaheri et al. [49] described a similar phenomenon. Strong sintering and rapid grain growth was reported already at temperatures of 650 and 800 °C,

respectively.

Table 4 summarizes the amount of the different starting powders in the final powder combinations for laser processing. The thermal treated granules were mixed with 30 vol% coarse alumina to break formed sintering necks in between thermal treated granules [23].

Table 5 summarizes the apparent density, tapped density and Hausner ratio of spray dried and thermal treated granules. The powder densities are lower before thermal treatment and consecutive mixing with the coarse aluminum oxide AA18. However, the flowability of these granules was in general better compared to the final thermal treated and mixed powders. This increase of density and Hausner ratio by thermal treatment and consecutive mixing with the coarse alumina was already described in [23]. Granules sintered together during thermal treatment (satellite formation) could be separated by addition of AA18 and thus, a denser packing of the powder was guaranteed. Despite this separation, the rapid grain growth at high temperatures (Fig. 3) led to a lower apparent and tapped density caused by deterioration of the sphericity for granules containing 14.3 vol% and 68 mol% (61.9 vol%) TiO_{2-x}.

The flowability of the different granules was also rated by the avalanche angle (Table 6). The spray-dried granules with the lowest amount of TiO_2 (1 vol%) showed the smallest avalanche angle of 32.9° ± 1.8° in the dynamic flow measurements. Pure granules with amount of 14.3 vol% and 68 mol% (61.9 vol%) TiO_2 gave an avalanche angle of 37.7 ± 2.3° and 37.3 ± 2.9°. This could be due to more irregular shaped (donut-shaped) granules impeding the flow by bridging [66]. Thermal treatment in Ar/H_2 had different consequences for the different addition amounts of titanium oxide. The avalanche angle of the granules containing 14.3 vol% of TiO_{2-x} only increased up to 45.2° for a maximum
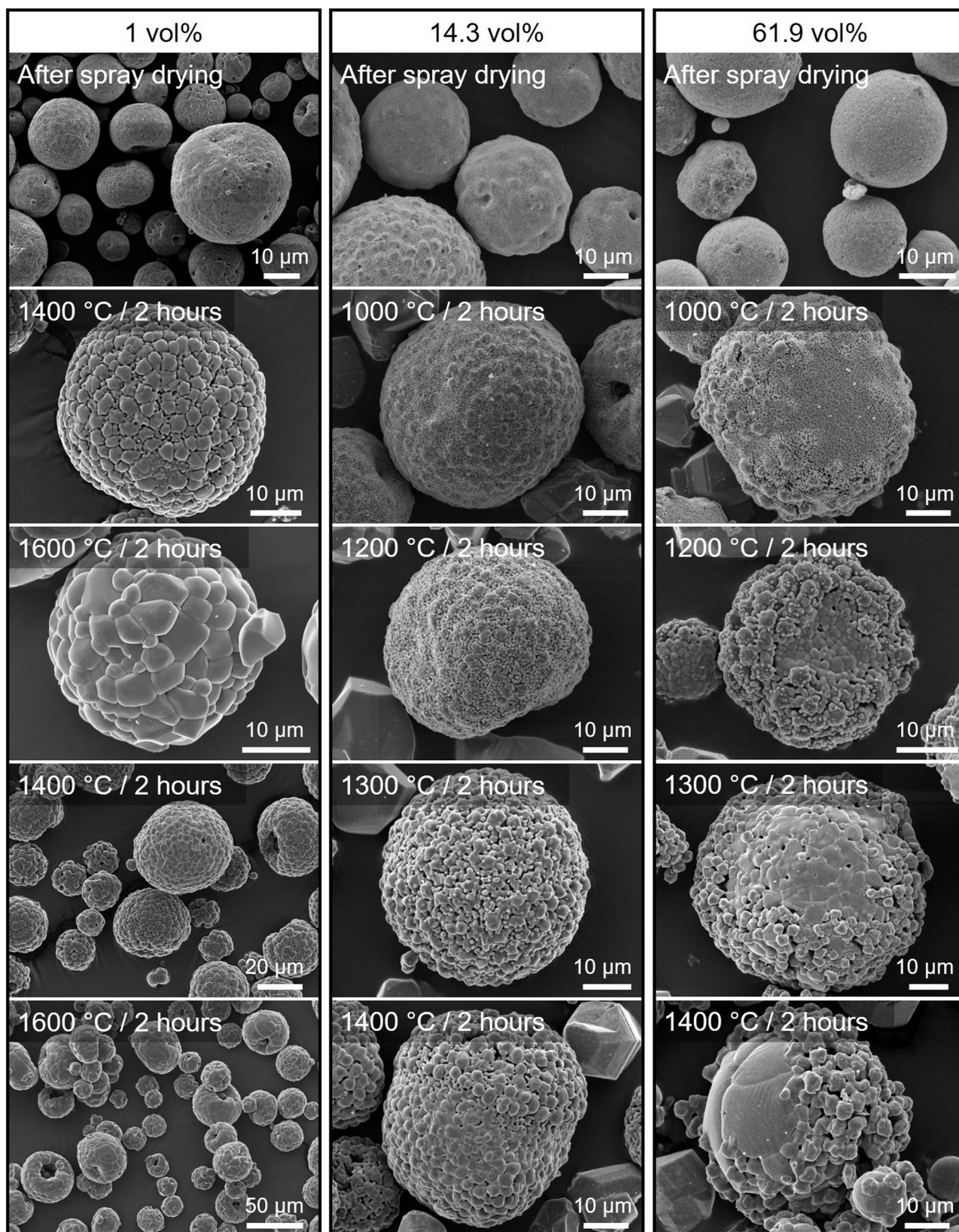
Fig. 3. SEM images of spray dried granules containing 1 vol%, 14.3 vol% and 61.9 vol% (68 mol%) of TiO_{2-x} before and after thermal treatment in Ar/H_2 at maximum temperatures (dwell time: 2 h) of 1000 °C, 1200 °C, 1300 °C, 1400 °C and 1600 °C (thermal treated granules are partially mixed with coarse AA18).

Table 4

Combinations of aluminum oxide and titanium oxide starting powders in the final powders for laser processing.

Amount of TiO2 within final powder for laser processing	Al2O3 AA18		Al2O3 AA3		Al2O3 Taimicron TM-DAR		Aeroxide TiO2 P25	
	vol %	wt %	vol %	wt %	vol %	wt %	vol %	wt %
0.7 vol%	30.0	30.0	50.3	50.5	19.0	18.8	0.7	0.7
10 vol%	30.0	29.9	50.8	50.8	9.2	9.1	10.0	10.2
50 mol% (43.4 vol%)	30.0	29.6	26.7	26.5	–	–	43.3	43.9

Table 5

Properties of spray dried granules and thermal treated granules.

a)	Spray-dried granules			
	Content of TiO$_{2-x}$	Apparent density [% of TD]	Tapped density [% of TD]	Hausner ratio
	1 vol%	40.1	45.5	1.14
	14.3 vol%	35.5	39.7	1.12
	68 mol%	23.6	27.2	1.15
b)	Thermal treated granules with 1 vol% TiO$_{2-x}$ mixed with 30 vol% coarse alumina AA18			
	Maximum temperature / dwell time of treatment in Ar/H$_2$	Apparent density [% of TD]	Tapped density [% of TD]	Hausner ratio
	1400 °C / 2 h	44.3	53.6	1.21
	1600 °C / 2 h	47.9	54.9	1.15
c)	Thermal treated granules with 14.3 vol% TiO$_{2-x}$ mixed with 30 vol% coarse alumina AA18			
	Maximum temperature / dwell time of treatment in Ar/H$_2$	Apparent density [% of TD]	Tapped density [% of TD]	Hausner ratio
	1000 °C / 2 h	37.4	44.5	1.19
	1200 °C / 2 h	38.4	46.6	1.21
	1300 °C / 2 h	41.0	49.2	1.20
	1400 °C / 2 h	40.3	49.4	1.23
d)	Thermal treated granules with 68 mol% (61.9 vol%) TiO$_{2-x}$ mixed with 30 vol% coarse alumina AA18			
	Maximum temperature / dwell time of treatment in Ar/H$_2$	Apparent density [% of TD]	Tapped density [% of TD]	Hausner ratio
	1000 °C / 2 h	35.0	42.8	1.22
	1100 °C / 2 h	33.7	41.9	1.24
	1200 °C / 2 h	37.1	45.6	1.23
	1300 °C / 2 h	37.3	44.8	1.20
	1400 °C / 2 h	34.5	43.5	1.26

Table 6

Comparison of the avalanche angles and Hausner ratios of in terms of the impact on the flowability by thermal treatment in Ar/H2 and mixing with 30 vol% coarse aluminum oxide AA18.

a)	Granules doped with 1 vol% TiO$_{2-x}$	Avalanche angle [deg]	Hausner ratio
	spray-dried granules	32.9	1.14
	treated at 1400 °C/2 h in Ar/H2	61.2	1.25
	treated at 1600 °C/2 h in Ar/H2	57.3	1.18
	treated at 1400 °C/2 h in Ar/H2 + 30 vol% AA18	48.0	1.21
	treated at 1600 °C/2 h in Ar/H2 + 30 vol% AA18	49.2	1.15
b)	Granules doped with 14.3 vol% TiO$_{2-x}$	Avalanche angle [deg]	Hausner ratio
	spray-dried granules	37.7	1.12
	treated at 1300 °C/2 h in Ar/H2	45.2	1.19
	treated at 1300 °C/2 h in Ar/H2 + 30 vol% AA18	48.3	1.21
c)	Granules doped with 68 mol% (61.9 vol%) TiO$_{2-x}$	Avalanche angle [deg]	Hausner ratio
	spray-dried granules	37.3	1.15
	treated at 1200 °C/2 h in Ar/H2	57.2	1.13
	treated at 1400 °C/2 h in Ar/H2	62.0	1.38
	treated at 1200 °C/2 h in Ar/H2 + 30 vol% AA18	54.5	1.23
	treated at 1400 °C/2 h in Ar/H2 + 30 vol% AA18	53.2	1.26

% (61.9 vol%) TiO$_2$ due the optimized ratio of apparent and tapped density as well as flowability. For 1 vol% of TiO$_2$ a treatment temperature of 1400 °C was chosen due to the limited accessibility of the high temperature furnace.

Fig. 4 shows the qualitative absorption spectrum measured at room temperature by the Kubelka Munk method of untreated and reduced granules. Granules after spray dying as well as pure aluminum oxide AA18 offer no absorption at the relevant wavelength of 532 nm (green laser) and 1070 nm (IR laser). However, the reduced TiO$_{2-x}$-doped alumina granules showed an increased absorptance after reduction in Ar/H$_2$. The highest absorption was measured for reduced granules containing 68 mol% (61.9 vol%) of titanium oxide, which is due to the highest amount of blackish TiO$_{2-x}$ within the granules after thermal treatment. The K/S ratio (absorption coefficient K divided by scattering coefficient S) decreased over the complete wavelength range (300–1500 nm) for granules containing less reduced titanium oxide.

Table 7 summarizes the powder combinations used for laser processing. All powders contain 70 vol% of granules and 30 vol% of coarse aluminum oxide AA18. The final amounts of TiO$_{2-x}$ in the powder combinations A, B and C after mixing were 0.7 vol%, 10 vol% and 50 mol% (43.4 vol%), respectively.

Table 8 summarizes the properties of the used powders for laser processing in terms of the solid loading, yield, characteristic size values of d$_{10}$, d$_{50}$ and d$_{90}$, apparent and tapped density and Hausner ratio. Doped aluminum oxide powders with comparable properties led in our previous works to laser processed parts with high densities (>93.7%) [19,23]. The solid loadings decreased with an increasing content of nano-sized TiO$_2$. The highest yield of spray drying was achieved for powder combination B due to the lowest slurry viscosity. The d$_{10}$ and d$_{50}$ value were similar for all powder combinations. However, d$_{90}$ of powder combination A was more than 15 μm bigger than for the other powder combinations. This could be due the higher thermal treatment temperatures of 1400 °C leading to more undesirable satellite formation.

X-ray diffraction confirmed the formation of reduced titanium oxide within the granules of powder combination C containing 50 mol% (43.4 vol%) TiO$_{2-x}$ (Fig. 5). Titanium oxide changed from predominantly anatase and partially rutile to reduced TiO$_{2-x}$ and rutile already for a maximum Ar/H$_2$ treatment temperature of 1000 °C. A treatment

temperature of 1300 °C. These granules sinter only slightly at this temperature with almost no change in shape. In comparison, the avalanche angles of the granules containing the other additive amounts increased close to the critical value of 60° [59], which represents the limit of the flowability suitable for the PBF-LB process. This over-sintering worsened the flowability by forming irregular shaped granules and satellite-shaped constructions. Addition of the coarse AA18 decreased the avalanche angle by more than 7.5° acting as flowable medium for the granules and separating satellite formations as also seen in [19,23]. However, the avalanche angle of the less-sintered granules containing 14.3 vol% of TiO$_{2-x}$ increased by 3.1°, since the edged shape of AA18 (avalanche angle of 44.6°) limited a further flowability improvement.

The avalanche angle (dynamic characterization method) and the Hausner ratio (static measurement) were in general comparable. Only a few powders with a high avalanche angle had a low Hausner ratio. However, the avalanche angles provide a more reliable measure of the flowability due the higher amount of test repetitions.

For further experiments, the thermal treatment temperatures of 1300 °C and 1200 °C were used for granules with 14.3 vol% and 68 mol
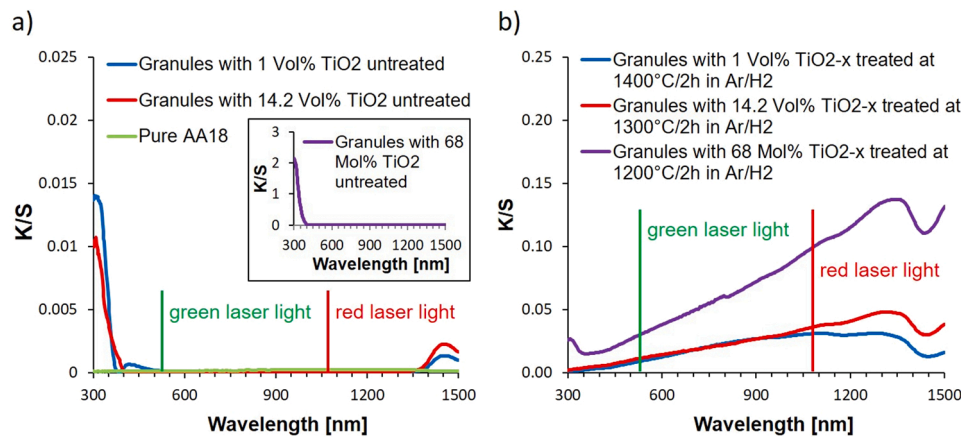
Fig. 4. Qualitative absorption spectrum at room temperature measured by the Kubelka Munk method of a) untreated granules and AA18 particles as well as of b) reduced granules.

Table 7
Powder combinations used for laser processing.

Powder combination	Content				Total Content of TiO$_{2-x}$ in powders for laser processing
A	70 vol %	Granules with 1 vol% TiO$_{2-x}$ thermally treated at 1400 °C for 2 h in Ar/H$_2$	30 vol %	Coarse aluminum oxide AA18	0.7 vol%
B	70 vol %	Granules with 14.3 vol % TiO$_{2-x}$ thermally treated at 1300 °C for 2 h in Ar/H$_2$	30 vol %	Coarse aluminum oxide AA18	10 vol%
C	70 vol %	Granules with 68 mol % (61.9 vol %) TiO$_{2-x}$ thermally treated at 1200 °C for 2 h in Ar/H$_2$	30 vol %	Coarse aluminum oxide AA18	50 mol% (43.4 vol%)

Table 8
Properties of powder combinations A, B and C.

Powder combination	A	B	C
Solid load in slurry [vol%]	49.4	30.0	10.4
Yield of spray drying [wt%]	22.0	66.9	32.5
Apparent density [% of TD]	44.3	41.0	37.1
Tapped density [% of TD]	53.6	49.2	45.6
Hausner ratio	1.21	1.20	1.23
d10 [μm]	16.8	17.5	15.5
d50 [μm]	33.2	34.8	32.2
d90 [μm]	73.0	56.4	57.6

with a maximum temperature of 1400 °C further transformed a significant part of the reduced titanium oxide and aluminum oxide to aluminum titanate (Al$_2$TiO$_5$).

3.3. Laser manufacturing of parts

3.3.1. Powder combination A

Attenuation contrast tomographic microscopy images showed a high number of cracks (highlighted in black in Fig. 6c) and development of micropores (highlighted in bright green in Fig. 6a, b) during laser processing of powder combination A. XRD-contrast tomography was performed to analyze the surroundings of the bubbles. A detailed description is given in the supplementary information (Fig. S1). The evaluated parts density and cracks density from these measurements for three different laser scanning speeds (2 mm/s, 5 mm/s, 10 mm/s) are depicted in Fig. 6d. The other process parameters given in the experimental section were kept constant. The crack density was calculated using following equation:

$$Cracks\ density = \frac{SA_{cracks}}{V\ x\ \rho} \tag{3}$$

where SA$_{cracks}$, V and ρ represent the total crack surface area in the measured volume in μm^2, the measured part volume in μm^3 and the density of the part in % of the theoretical density, respectively.

An increasing scanning speed led to a decrease in cracks density and part density of the laser printed alumina parts. The part density decreases due to lower temperatures within the melt-pool, which were not sufficient for a complete consolidation of the used powder. However, the increasing porosity was beneficial for crack reduction, since the material could shrink with experiencing less tensile stresses during the cooling phase. Finally, the conclusion could be drawn that a doping amount of 0.7 vol% TiO$_{2-x}$ was not effective to reduce cracks in PBF-LB of alumina. In comparison to parts produced from aluminum oxide powders containing a similar amount of manganese oxide or iron oxide dopant (developed in the authors' previous works [4,19,23]) using the same processing conditions, no clear trend was seen for the influence on the cracks and part density (Fig. S2).

3.3.2. Powder combination B and C

A processing window was found for both powder combinations building 6 × 6 × 6 mm cubes (Fig. 7).

For the powders containing 10 vol% titanium oxide only few parameters led to good results even though a large window of parameters was explored between 30 and 80 W and between 50 and 360 mm/s. The production of cylinders with this powder was difficult, because parts were always thermally distorted and had major defects when a circular cross-section was built. Instead, the processing window for the powders with 50 mol% (43.4 vol%) titanium oxide was much wider and led easily to the production of cylinders for the compression tests. The used spot size, hatch distance, layer thickness and substrate given in the
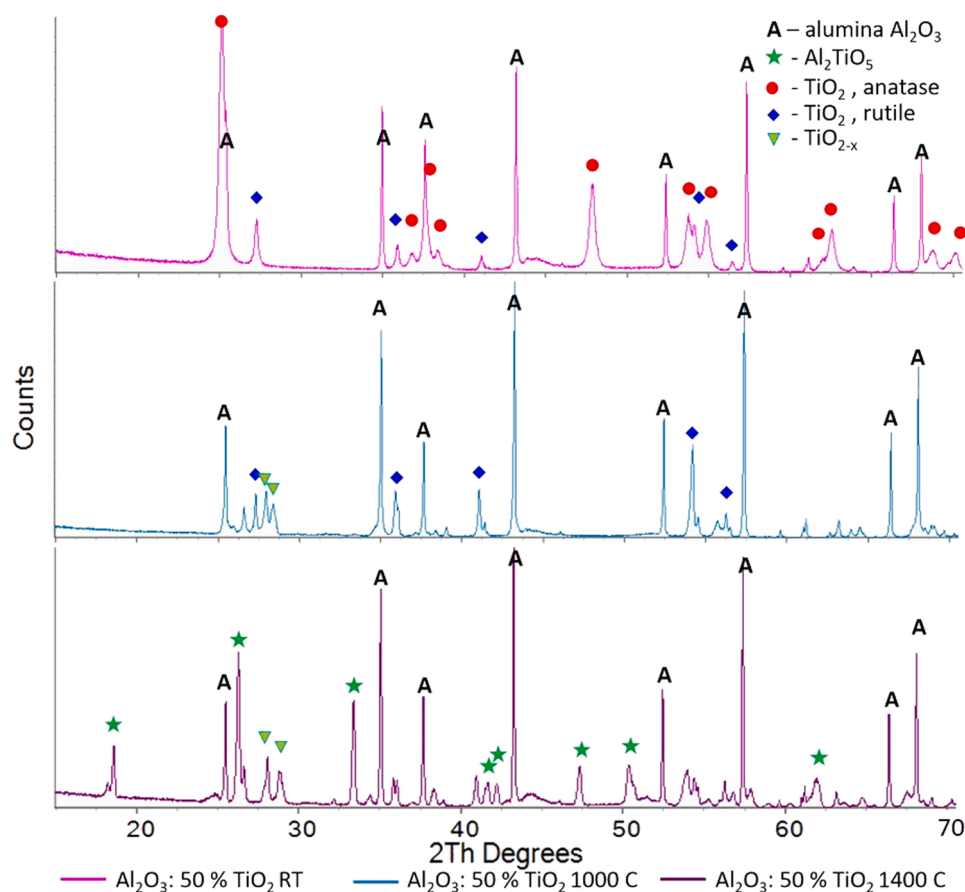
Fig. 5. X-ray diffraction measurements of powder combination C (50 mol% (43.4 vol%) of TiO_{2-x}) before and after thermal treatment in Ar/H_2 at maximum temperatures (dwell time: 2 h) of 1000 °C and 1400 °C.

experimental section were kept constant for both powders: A laser power of 40 W and a scan speed of 80 mm/s for powder combination B (10 vol% TiO_{2-x}) and a laser power of 30 W and a scan speed of 70 mm/ s for powder combination C (43.4 vol% TiO_{2-x}) were chosen for further processing, since the parts processed with these process parameters showed the highest density and accuracy.

Fig. 8 shows the internal structure of laser manufactured parts produced with powder combination B. A deformation was visible on the upper side, which was probably due to the denudation caused by the flow of powder inside the melt pool. The parts were homogeneously consolidated by the IR laser achieving a part density of 94.0%. However, various laser-induced cracks generated by thermal shock due to thermal gradients during cooling were seen in the cross-sections (view of build direction Fig. 8a-d and top view Fig. 8e, f). The frequency of the cracks was approximately similar to the hatch distance, which could mean that a crack is generated at every scan track. A similar situation was also observed by Ferrage et al. [15]. They found a columnar structure defined by cracks on both sides in cross-section micrographs, which was approximately in the same size of the hatch distance. Furthermore, the microstructure revealed a small amount of circular pores (Fig. 8c) and unmolten particles within the pores (Fig. 8d). A crack reduction by the formation of aluminum titanate was not given in this case.

The shape of a laser-manufactured part produced with powder combination C is imaged by optical microscopy in Fig. 9a. The accuracy of the lateral areas is high, whereas the top surface has a slightly wavy appearance. Furthermore, the internal structure is presented in build direction and from the top view (Fig. 9a-e). The parts were uniformly consolidated by the IR laser with a low amount of micron-sized pores leading to a part density of 96.5%. Laser-induced cracks were strongly reduced in these parts and could be only found in higher magnifications

of the cross-sections. The cracks appear narrower compared to parts processed from powder combination B. The cracks are particularly small in width and they are irregular, which led to cracks mainly distributed along the building direction. The microstructure is particularly uniform and no grains or phase segregation could be observed.

The total content of 50 mol% (43.4 vol%) TiO_{2-x} in powder combination C leads to improved laser manufactured parts in terms of reduction of severe cracks compared to power combination A and B. The in-situ reaction of aluminum oxide and titanium oxide to the ternary phase aluminum titanate, which has a low Young's modulus, a low thermal expansion coefficient, low thermal conductivity and therefore, an excellent thermal shock behavior [32,33], leads to this crack reduction. However, the volume expansion, caused by the aluminum titanate formation from the well-dispersed alumina and titania particles, can also lead to crack formation during the rapid cooling process. The temporal evolution of this phase could be further analyzed in the future by in-situ X-ray diffraction as shown by Hocine et al. for PBF-LB of Ti-6Al-4 V [67].

Crack-free parts were already manufactured by directed energy deposition (DED) using aluminum oxide and titanium oxide powders. The amount of cracks was reduced proportionally to the amount of the additive [29], similar to the results in this work. However, the amount of 50 mol% titanium oxide exceeds by far the amount of 10.5 mol%, which was stated in several references about laser cladding as most suitable to achieve layers without cracks and porosity [36–38]. This could be due to a different temperature distribution around the melt pool in DED and laser cladding, which is usually done by irradiation of the substrate and a subsequent powder addition into the molten pool. This method requires in general a laser spot diameter, which is ca. one order of magnitude larger than in PBF-LB and therefore, bigger and more homogenous temperature areas can be consolidated simultaneously
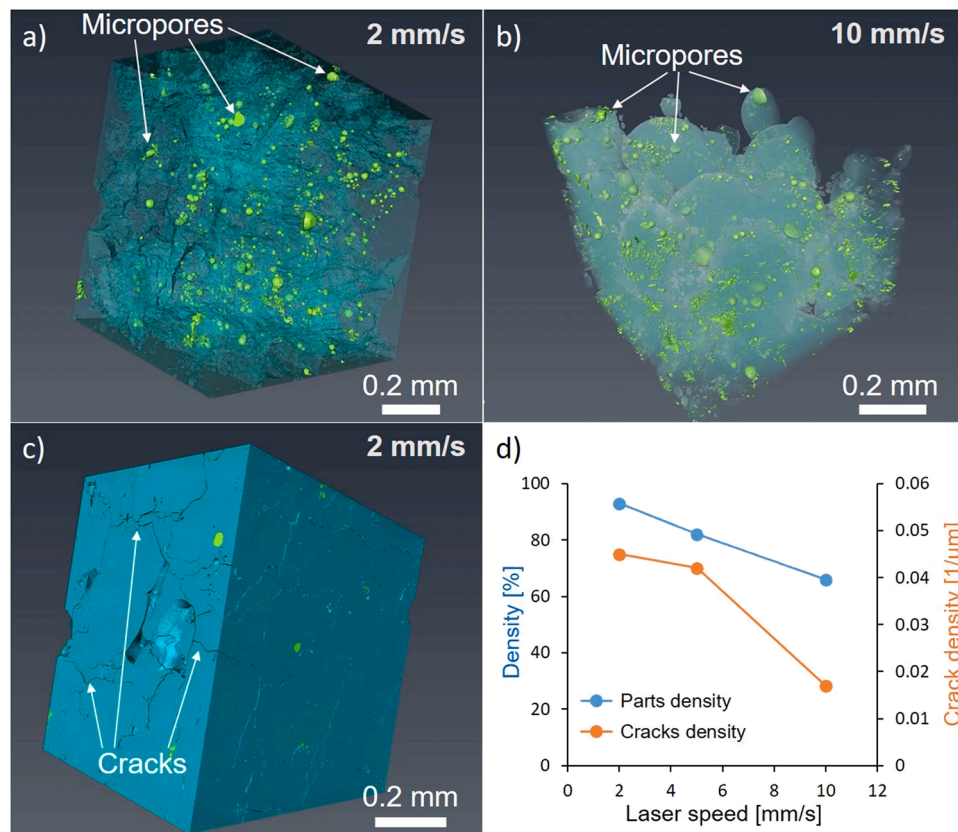
Fig. 6. a), b), c) Attenuation contrast tomographic microscopy of laser printed parts. d) Evaluation of parts density and cracks density at different laser scanning speeds (2 mm/s, 5 mm/s, 10 mm/s).
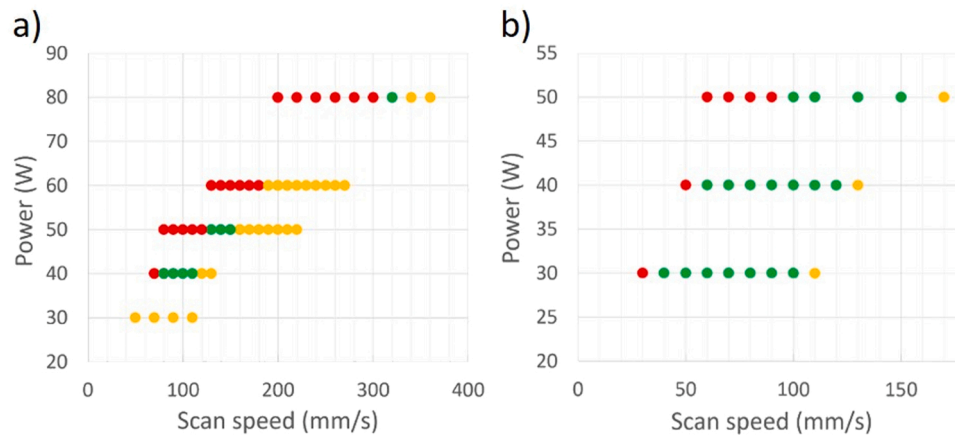

Fig. 7. a) laser process window for powders containing 10 vol% titanium oxide (powder combination B) and b) laser process window for powders containing 50 mol % (43.4 vol%) titanium oxide (powder combination B). (Red: overmelted parts. Yellow: balling or other major defects. Green: stable parts without major visible defects.).

compared to traditional PBF-LB leading to less thermal stresses.

X-ray diffraction measurements (Fig. 10) showed that the desired Al_2TiO_5 formation was achieved in the PBF-LB printed parts made from powders containing 10 vol% of TiO_{2-x} and 50 mol% (43.4 vol%) TiO_{2-x}. The parts made from powder combination C featured the majority of Al_2TiO_5 in the crystalline phase. However, a complete transformation of aluminum oxide and titanium oxide to aluminum titanate did not occur during laser processing.

3.4. Mechanical properties

Laser processing using powders containing 10 vol% and 50 mol% (43.4 vol%) of reduced titanium oxide (powder combination B and C) gave parts with compressive strength values of 138.0 ± 31.2 MPa and 346.6 ± 47.9 MPa, respectively. The strength of the parts increased with the amount of used titanium oxide additive. This shows that the crack reduction due to the in-situ formation of aluminum titanate has a great impact on the strength improvement. A low compressive strength was expected with a higher amount of generated aluminum titanate, since this material has only a compressive strength of 200 MPa [68], whereas
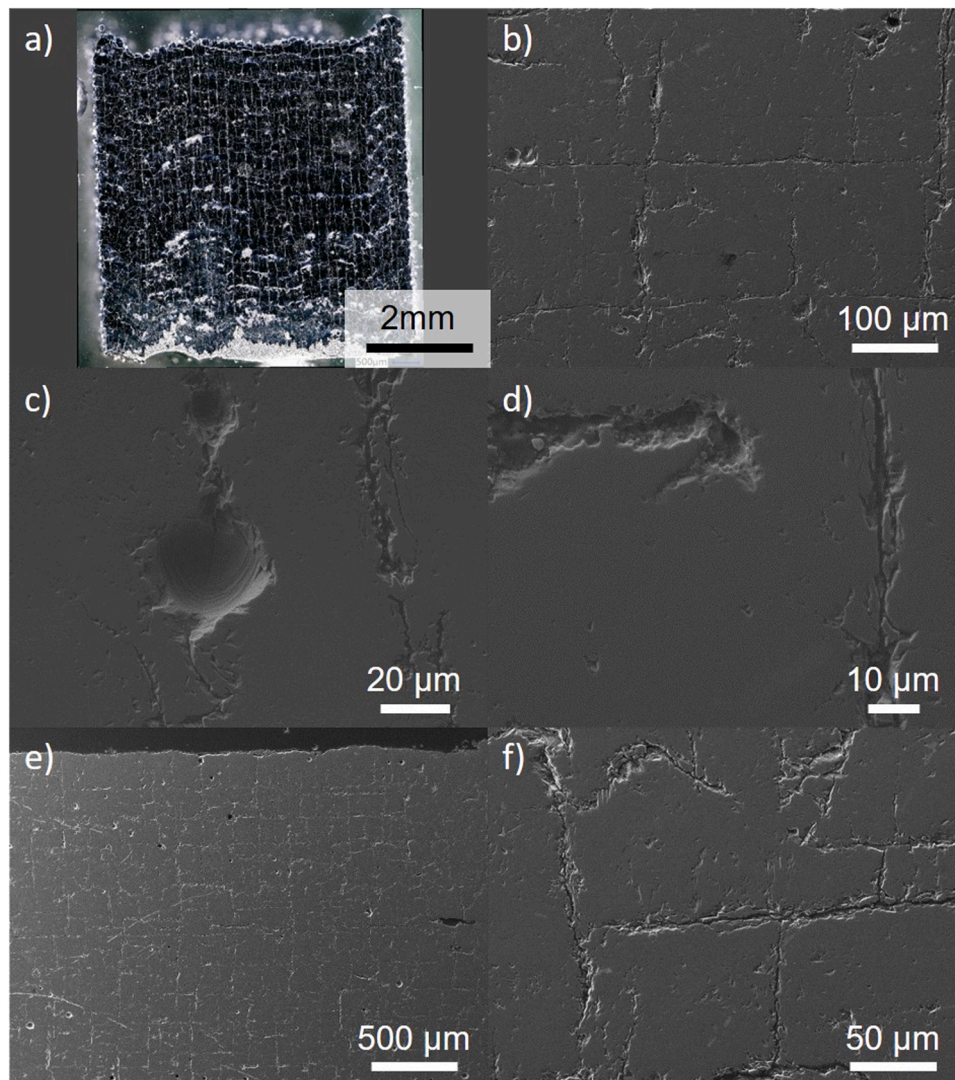
Fig. 8. Internal structure imaged by optical microscopy and SEM of laser manufactured parts produced with powder combination B. a) - d) Build direction view and f), g) top view of cross-sections.

compressive stresses of traditional processed aluminum oxide parts can exceed 4000 MPa (depending on the used grain size, purity of the raw material and the production method) [69]. Severe crack formation due to thermal stresses during the rapid cooling in laser processing reduces in general this strength [70].

Furthermore, these parts made from powder combination C showed an improved compressive strength compared to laser-processed parts made from aluminum oxide granules doped with 0.6 vol% iron oxide [4, 19,23]. A compressive strength of only 219.3 ± 45.7 MPa was measured for these parts. Other comparable compressive strength values of laser-manufactured parts were found in Exner et al. [5,71]. They achieved 800 MPa directly after laser processing and 1150 MPa after annealing using glass-ceramic composite materials. Partially molten amorphous silica with a low thermal expansion coefficient reduced the crack formation [72]. However, these parts were finally limited to the strength of the glass phase.

The measured Young's moduli of the parts made from powder combination B and C were 21.4 and 90.2 GPa, respectively. These low Young's moduli were obtained due to the appearance of Al_2TiO_5 with a Young's modulus of only 14 GPa [33], which is by far lower than the Young's modulus of Al_2O_3 (410 GPa) [73]. Contrary to the expected values, the parts made with powder combination C showed a higher Young's modulus than the parts processed with powders combination B,

despite having a higher phase content of aluminum titanate. This can be explained by the higher amount of porosity [73] and apparent cracks in the microstructure [74,75], which strongly reduce the Young's modulus.

4. Conclusions

Reduced titanium oxide was shown as a suitable additive to reduce crack formation in laser powder bed fusion of aluminum oxide by the in-situ formation of aluminum titanate. This phase offers a low Young's modulus and a low thermal expansion coefficient.

A thermal gravimetric analysis revealed that reduction of TiO_2 to TiO_{2-x} in argon/hydrogen atmosphere initiated at 980 °C. The color change from white to blackish upon reduction enabled laser processing in the visible or near-infrared range of the light. Thermal treatment temperatures of 1400 °C, 1300 °C and 1200 °C were found as the most suitable temperatures for granules with 1 vol%, 14.3 vol% and 68 mol% (61.9 vol%) TiO_2, respectively. These granules needed to be mixed with coarse alumina after thermal treatment to break sintering necks in between the granules and therefore, to increase the apparent density, tapped density as well as to decrease the flowability (avalanche angle and Hausner ratio) to a suitable level. The final powders used for laser processing contained 0.7 vol%, 10 vol% and 50 mol% (43.4 vol%) TiO_{2-x}.
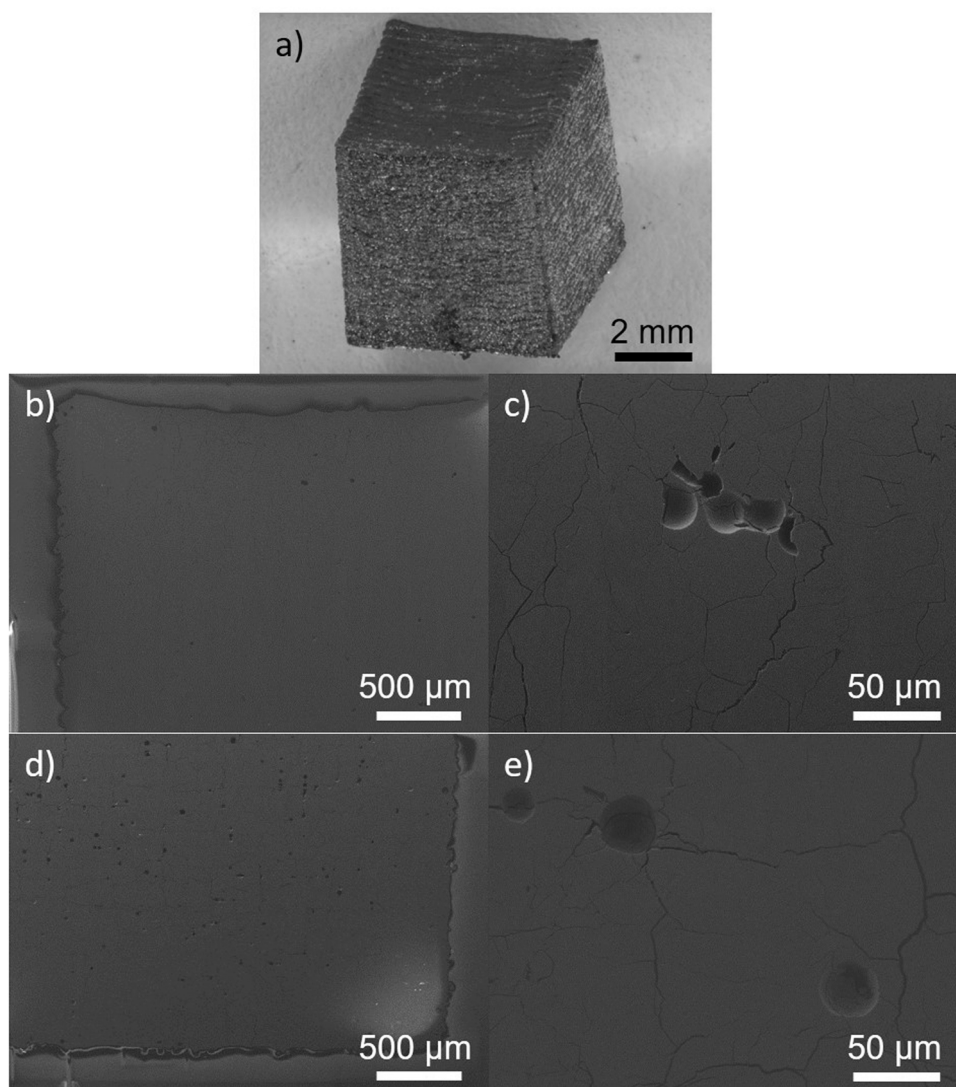
Fig. 9. a) Shape imaged by optical microscopy. Internal structure imaged by SEM of cross-sections (b), c) view in build direction and d), e) top view of laser manufactured parts produced with powder combination C.
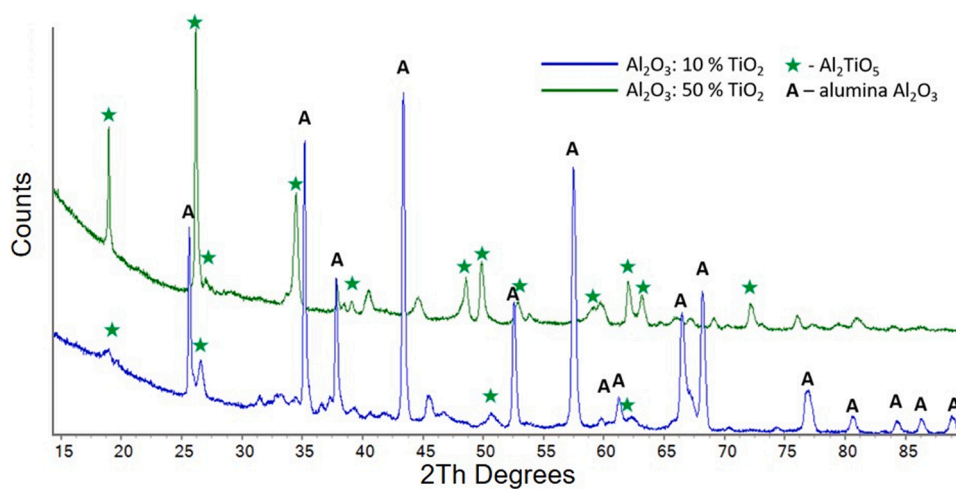

Fig. 10. X-ray diffraction measurements of laser processed parts made from powder combination B (10 vol% of TiO_{2-x}) and powder combination C (50 mol% (43.4 vol%) of TiO_{2-x}).

Tomographic microscopy revealed a severe crack formation by laser processing for the low dopant amount of 0.7 vol% TiO_{2-x}. A higher amount of 10 vol% TiO_{2-x} was not helpful to reduce the cracks upon PBF-LB due to the lack of sufficient in-situ formed aluminum titanate. The total content of 50 mol% (43.4 vol%) TiO_{2-x} led to improved parts due the formation of this ternary phase with an excellent thermal shock behavior. Laser processing with this powder gave parts with a density of 96.5% of the theoretical density, a compressive strength of 346.6 $\pm$ 47.9 MPa and Young's modulus of 90.2 GPa.

Despite the positive effect of the presence of Al_2TiO_5 on the crack formation, too high a quantity with a low mechanical strength can be counterproductive for the final strength of the laser manufactured parts. More ratios of aluminum oxide to reduced titanium oxide should be tested in the future to find an optimized compromise between the advantages and disadvantages given by the in-situ formed aluminum titanate phase.

Declaration of Competing Interest

The authors declare that they have no known competing financial interests or personal relationships that could have appeared to influence the work reported in this paper.

Acknowledgements

Appendix A. Supporting information

Supplementary data associated with this article can be found in the online version at doi:10.1016/j.jeurceramsoc.2022.02.046.

References

[1] S. Pfeiffer, K. Florio, D. Puccio, M. Grasso, B.M. Colosimo, C.G. Aneziris, K. Wegener, T. Graule, Direct laser additive manufacturing of high performance oxide ceramics: a state-of-the-art review, J. Eur. Ceram. Soc. 41 (13) (2021) 6087–6114.

[2] A. Gahler, J.G. Heinrich, J. Günster, Direct laser sintering of Al2O3-SiO2 dental ceramic components by layer-wise slurry deposition, J. Am. Ceram. Soc. 89 (10) (2006) 3076–3080.

[3] J. Deckers, S. Meyers, J.P. Kruth, J. Vleugels, Direct selective laser sintering/melting of high density alumina powder layers at elevated temperatures, Phys. Procedia 56 (2014) 117–124.

[4] K. Florio, S. Pfeiffer, M. Makowska, N. Casati, F. Verga, T. Graule, H. Van Swygenhoven, K. Wegener, An innovative selective laser melting process for hematite-doped aluminum oxide, Adv. Eng. Mater. 21 (6) (2019).

[5] P. Regenfuss, A. Streek, L. Hartwig, S. Klötzer, T. Brabant, M. Horn, R. Ebert, H. Exner, Principles of laser micro sintering, Rapid Prototyp. J. 13 (4) (2007) 204–212.

[6] Z. Fan, M. Lu, H. Huang, Selective laser melting of alumina: a single track study, Ceram. Int. 44 (8) (2018) 9484–9493.

[7] J. Liu, S. Bai, Femtosecond laser additive manufacturing of YSZ, Appl. Phys. A 123 (4) (2017).

[8] Y. Zheng, K. Zhang, T.T. Liu, W.H. Liao, C.D. Zhang, H. Shao, Cracks of alumina ceramics by selective laser melting, Ceram. Int. 45 (1) (2019) 175–184.

[9] S. Buls, J. Vleugels, B. Van Hooreweder, Microwave assisted selective laser melting of technical ceramics, Annual international solid freeform fabrication symposium - an additive manufacturing conference 29 (2018) 2349–2357.

[10] Y.-C. Hagedorn, J. Wilkes, W. Meiners, K. Wissenbach, R. Poprawe, Net shaped high performance oxide ceramic parts by selective laser melting, Phys. Procedia 5 (2010) 587–594.

[11] Q. Liu, Y. Danlos, B. Song, B. Zhang, S. Yin, H. Liao, Effect of high-temperature preheating on the selective laser melting of yttria-stabilized zirconia ceramic, J. Mater. Process. Tech. 222 (2015) 61–74.

[12] B.H. Bae, J.W. Lee, J.M. Cha, I.-W. Kim, H.-D. Jung, C.-B. Yoon, Preliminary characterization of glass/alumina composite using laser powder bed fusion (L-PBF) additive manufacturing, Materials 13 (9) (2020) 2156.

[13] N.K. Tolochko, Y.V. Khlopkov, S.E. Mozzharov, M.B. Ignatiev, T. Laoui, V.I. Titov, Absorptance of powder materials suitable for laser sintering, Rapid Prototyp. J. 6 (3) (2000) 155–161.

[14] E. Juste, F. Petit, V. Lardot, F. Cambier, Shaping of ceramic parts by selective laser melting of powder bed, J. Mater. Res. 29 (17) (2014) 2086–2094.

[15] L. Ferrage, G. Bertrand, P. Lenormand, Dense yttria-stabilized zirconia obtained by direct selective laser sintering, Addit. Manuf. 21 (2018) 472–478.

[16] S. Chang, L. Li, L. Lu, J.Y.H. Fuh, Selective laser sintering of porous silica enabled by carbon additive, Materials 10 (11) (2017).

[17] L. Moniz, C. Colin, J.-D. Bartout, K. Terki, M.-H. Berger, Laser beam melting of alumina: effect of absorber additions, JOM 70 (3) (2018) 328–335.

[18] F. Verga, M. Borlaf, L. Conti, K. Florio, M. Vetterli, T. Graule, M. Schmid, K. Wegener, Laser-based powder bed fusion of alumina toughened zirconia, Addit. Manuf. 31 (2020).

[19] S. Pfeiffer, K. Florio, M. Makowska, D. Ferreira Sanchez, H. Van Swygenhoven, C. G. Aneziris, K. Wegener, T. Graule, Iron oxide doped spray dried aluminum oxide granules for selective laser sintering and melting of ceramic parts, Adv. Eng. Mater. 21 (6) (2019).

[20] M. Makowska, S. Pfeiffer, N. Casati, K. Florio, M. Vetterli, K. Wegener, T. Graule, H. van Swygenhoven, Pre-processing of hematite-doped alumina granules for selective laser melting, Ceram. Int. 45 (14) (2019) 17014–17022.

[21] X. Zhang, S. Pfeiffer, P. Rutkowski, M. Makowska, D. Kata, J. Yang, T. Graule, Laser cladding of manganese oxide doped aluminum oxide granules on titanium alloy for biomedical applications, Appl. Surf. Sci. 520 (2020), 146304.

[22] K. Florio, D. Puccio, G. Viganò, S. Pfeiffer, F. Verga, M. Grasso, B.M. Colosimo, T. Graule, K. Wegener, Process characterization and analysis of ceramic powder bed fusion, Int. J. Adv. Manuf. Technol. (2021).

[23] S. Pfeiffer, M. Makowska, F. Kevin, D.F. Sanchez, F. Marone, X. Zhang, C. G. Aneziris, H. Van Swygenhoven, K. Wegener, T. Graule, Selective laser melting of thermal pre-treated metal oxide doped aluminum oxide granules, Open Ceram. (2020), 100007.

[24] B. Qian, Z. Shen, Laser sintering of ceramics, J. Asian Ceram. Soc. 1 (4) (2013) 315–321.

[25] P. Bertrand, F. Bayle, C. Combe, P. Goeuriot, I. Smurov, Ceramic components manufacturing by selective laser sintering, Appl. Surf. Sci. 254 (4) (2007) 989–992.

[26] M. Mapar, D.Q. Zhang, Z.H. Liu, W.Y. Yeong, C.K. Chua, B.Y. Tay, O. Geramifard, S. Maleksaeedi, F.E. Wiria, Preparation and flowability characterization of ceramic powders for selective laser melting, High value manufacturing: Advanced research in virtual and rapid prototyping, Leira,PT, 2014, pp. 267–271.

[27] M. Mapar, Selective Laser Melting of Ceramic-based Materials for Dental Applications, Nanyang Technological University, 2014.

[28] H. Liu, H. Su, Z. Shen, E. Wang, D. Zhao, M. Guo, Z. Zhang, L. Liu, H. Fu, Direct formation of Al2O3/GdAlO3/ZrO2 ternary eutectic ceramics by selective laser melting: microstructure evolutions, J. Eur. Ceram. Soc. 38 (15) (2018) 5144–5152.

[29] F. Niu, D. Wu, Y. Huang, S. Yan, G. Ma, C. Li, J. Ding, Direct additive manufacturing of large-sized crack-free alumina/aluminum titanate composite ceramics by directed laser deposition, Rapid Prototyp. J. (2019).

[30] D. Wu, Y. Huang, F. Niu, G. Ma, S. Yan, C. Li, J. Ding, Effects of TiO2 doping on microstructure and properties of directed laser deposition alumina/aluminum titanate composites, Virt. Phys. Prototyp. 14 (5) (2019) 371–381.

[31] Y. Huang, D. Wu, D. Zhao, F. Niu, H. Zhang, S. Yan, G. Ma, Process optimization of melt growth alumina/aluminum titanate composites directed energy deposition: effects of scanning speed, Addit. Manuf. (2020), 101210.

[32] Y. Ohya, S. Yamamoto, T. Ban, M. Tanaka, S. Kitaoka, Thermal expansion and mechanical properties of self-reinforced aluminum titanate ceramics with elongated grains, J. Eur. Ceram. Soc. 37 (4) (2017) 1673–1680.

[33] I.J. Kim, H. Supkwak, Thermal shock resistance and thermal expansion behaviour with composition and microstructure of Al2TiO5 ceramics, Can. Metall. Q. 39 (4) (2000) 387–396.

[34] N.P. Padture, S.J. Bennison, H.M. Chan, Flaw-tolerance and crack-resistance properties of alumina-aluminum titanate composites with tailored microstructures, J. Am. Ceram. Soc. 76 (9) (1993) 2312–2320.

[35] S. Bueno, M.-H. Berger, R. Moreno, C. Baudín, Fracture behaviour of microcrack-free alumina–aluminium titanate ceramics with second phase nanoparticles at alumina grain boundaries, J. Eur. Ceram. Soc. 28 (10) (2008) 1961–1971.

[36] Y. Chen, D. Wu, G. Ma, W. Lu, D. Guo, Coaxial laser cladding of Al2O3-13%TiO2 powders on Ti-6Al-4V alloy, Surf. Coat. Technol. 228 (2013) S452–S455.

[37] X.-s Gao, Z.-j Tian, Z.-d Liu, L.-d Shen, Interface characteristics of Al2O3-13%TiO2 ceramic coatings prepared by laser cladding, Trans. Nonferrous Met. Soc. China 22 (10) (2012) 2498–2503.

[38] D. Wang, Z. Tian, S. Wang, L. Shen, Z. Liu, Microstructural characterization of Al2O3–13wt% TiO2 ceramic coatings prepared by squash presetting laser cladding on GH4169 superalloy, Surf. Coat. Technol. 254 (2014) 195–201.

[39] H. Tang, F. Levy, H. Berger, P. Schmid, Urbach tail of anatase TiO 2, Phys. Rev. B 52 (11) (1995) 7771.

[40] H. Lu, B. Zhao, R. Pan, J. Yao, J. Qiu, L. Luo, Y. Liu, Safe and facile hydrogenation of commercial Degussa P25 at room temperature with enhanced photocatalytic activity, RSC Adv. 4 (3) (2014) 1128–1132.

[41] X. Chen, D. Zhao, K. Liu, C. Wang, L. Liu, B. Li, Z. Zhang, D. Shen, Laser-modified black titanium oxide nanospheres and their photocatalytic activities under visible light, ACS Appl. Mater. Interfaces 7 (29) (2015) 16070–16077.

[42] A. Kitada, G. Hasegawa, Y. Kobayashi, K. Kanamori, K. Nakanishi, H. Kageyama, Selective preparation of macroporous monoliths of conductive titanium oxides Ti n O2 n–1 (n= 2, 3, 4, 6), J. Am. Chem. Soc. 134 (26) (2012) 10894–10898.

[43] T. Ioroi, H. Kageyama, T. Akita, K. Yasuda, Formation of electro-conductive titanium oxide fine particles by pulsed UV laser irradiation, Phys. Chem. Chem. Phys. 12 (27) (2010) 7529–7535.

[44] X. Li, A.L. Zhu, W. Qu, H. Wang, R. Hui, L. Zhang, J. Zhang, Magneli phase Ti4O7 electrode for oxygen reduction reaction and its implication for zinc-air rechargeable batteries, Electrochim. Acta 55 (20) (2010) 5891–5898.

[45] I. Tsuyumoto, H. Uchikawa, New orthorhombic titanium oxide, TiO1. 94, J. Mater. Sci. Lett. 19 (23) (2000) 2075–2076.

[46] T. Lin, C. Yang, Z. Wang, H. Yin, X. Lü, F. Huang, J. Lin, X. Xie, M. Jiang, Effective nonmetal incorporation in black titania with enhanced solar energy utilization, Energy Environ. Sci. 7 (3) (2014).

[47] V. Adamaki, F. Clemens, P. Ragulis, S.R. Pennock, J. Taylor, C.R. Bowen, Manufacturing and characterization of Magnéli phase conductive fibres, J. Mater. Chem. A 2 (22) (2014) 8328–8333.

[48] R. Dittmann, E. Wintermantel, T. Graule, Sintering of nano-sized titania particles and the effect of chlorine impurities, J. Eur. Ceram. Soc. 33 (15–16) (2013) 3257–3264.

[49] M. Mazaheri, A. Zahedi, M. Haghighatzadeh, S. Sadrnezhaad, Sintering of titania nanoceramic: densification and grain growth, Ceram. Int. 35 (2) (2009) 685–691.

[50] R.K. McGeary, Mechanical packing of spherical particles, J. Am. Ceram. Soc. 44 (10) (1961) 513–522.

[51] P.C. Hidber, T.J. Graule, L.J. Gauckler, Citric acid—a dispersant for aqueous alumina suspensions, J. Am. Ceram. Soc. 79 (7) (1996) 1857–1867.

[52] J. Sauter, Die Grössenbestimmung der im Gemischnebel von Verbrennungskraftmaschinen vorhandenen Brennstoffteilchen: (Mitteilung aus dem Laboratorium für Technische Physik der Technischen Hochschule München), VDI-Verlag1926.

[53] K.F. Young, H.P.R. Frederikse, Compilation of the static dielectric constant of inorganic solids, J. Phys. Chem. Ref. Data 2 (2) (1973) 313–410.

[54] J.R. DeVore, Refractive indices of rutile and sphalerite, JOSA 41 (6) (1951) 416–419.

[55] J.-P. Choi, G.-H. Shin, H.-S. Lee, D.-Y. Yang, S. Yang, C.-W. Lee, M. Brochu, J.-H. Yu, Evaluation of powder layer density for the selective laser melting (SLM) process, Mater. Trans. 58 (2) (2017) 294–297.

[56] R. Engeli, T. Etter, S. Hövel, K. Wegener, Processability of different IN738LC powder batches by selective laser melting, J. Mater. Process. Tech. 229 (2016) 484–491.

[57] A. Amado, M. Schmid, G. Levy, K. Wegener, Advances in SLS powder characterization, Proceedings of the 22th Solid Freeform Fabrication Symposium, Austin, Texas, USA, 2011, pp. 438–452.

[58] J.-P. Choi, G.-H. Shin, S. Yang, D.-Y. Yang, J.-S. Lee, M. Brochu, J.-H. Yu, Densification and microstructural investigation of Inconel 718 parts fabricated by selective laser melting, Powder Technol. 310 (2017) 60–66.

[59] M. Vetterli, Powder optimization for laser sintering: An insight in powder intrinsic and extrinsic properties, ETH Zurich, Zurich, 2019.

[60] P. Kubelka, F. Munk, Ein Beitrag zur Optik der Farbanstriche (Contribution to the optic of paint), Z. Technol. Phys. 12 (1931) 593–601.

[61] J.M. Olinger, P.R. Griffiths, Quantitative effects of an absorbing matrix on near-infrared diffuse reflectance spectra, Anal. Chem. 60 (21) (1988) 2427–2435.

[62] K. Kendall, Adhesion: molecules and mechanics, Science 263 (5154) (1994) 1720–1725.

[63] M. Sathiyakumar, F.D. Gnanam, Influence of MnO and TiO2 additives on density, microstructure and mechanical properties of Al2O3, Ceram. Int. 28 (2) (2002) 195–200.

[64] F. Iskandar, L. Gradon, K. Okuyama, Control of the morphology of nanostructured particles prepared by the spray drying of a nanoparticle sol, J. Colloid Interface Sci. 265 (2) (2003) 296–303.

[65] G. Bertrand, C. Filiatre, H. Mahdjoub, A. Foissy, C. Coddet, Influence of slurry characteristics on the morphology of spray-dried alumina powders, J. Eur. Ceram. Soc. 23 (2) (2003) 263–271.

[66] J.S. Reed. Introduction to the Principles of Ceramic Processing, first ed., John Wiley & Sons, Inc, 1988.

[67] S. Hocine, H. Van Swygenhoven, S. Van Petegem, C.S.T. Chang, T. Maimaitiyili, G. Tinti, D. Ferreira Sanchez, D. Grolimund, N. Casati, Operando X-ray diffraction during laser 3D printing, Mater. Today 34 (2020) 30–40.

[68] Keranova AB ⟨http://www.keranova.se/Engelsk/Exceltabell_E.htm, 2006⟩. (Accessed 13 July 2021).

[69] P. Auerkari, Mechanical and physical properties of engineering alumina ceramics, 1996.

[70] J.F. Li, L. Li, F.H. Stott, Thermal stresses and their implication on cracking during laser melting of ceramic materials, Acta Mater. 52 (14) (2004) 4385–4398.

[71] H. Exner, M. Horn, A. Streek, F. Ullmann, L. Hartwig, P. Regenfuß, R. Ebert, Laser micro sintering: a new method to generate metal and ceramic parts of high resolution with sub-micrometer powder, Virt. Phys. Prototyp. 3 (1) (2008) 3–11.

[72] A.V. Gusarov, M. Pavlov, I. Smurov, Residual stresses at laser surface remelting and additive manufacturing, Phys. Procedia 12 (2011) 248–254.

[73] H. Salmang, H. Scholze, Keramik, Springer-Verlag Berlin Heidelberg Berlin Heidelberg 2007.

[74] Y. Ohya, Ze Nakagawa, K. Hamano, Crack healing and bending strength of aluminum titanate ceramics at high temperature, J. Am. Ceram. Soc. 71 (5) (1988). C-232-C-233.

[75] K. Hamano, Y. Ohya, Z.-e Nakagawa, Crack propagation resistance of aluminium titanate ceramics, Int. J. High. Technol. Ceram. 1 (2) (1985) 129–137.